

EXPLOITING THE REDUNDANCY IN SCANS WITH BOLOMETER ARRAYS

H. Roussel¹

Abstract. The scanning (on-the-fly) observing mode is the most efficient for a wide range of mapping applications, but requires special processing techniques. This short article presents an algorithm designed to make use of the redundancy built in scan observations to subtract instrumental (or atmospheric) brightness drifts. Each point of the sky being scanned by several bolometers, at several times distributed over a significant fraction of the total observation duration, drifts can be extracted from the data with no a-priori knowledge of the noise characteristics and a minimal knowledge of the instrument.

Keywords: astronomical instrumentation, data processing, infrared, submillimeter

1 Introduction

Observations with bolometer arrays are affected by additive drifts, caused by low-frequency noise. If left uncorrected, the thermal part of this noise may strongly distort extended emission; the non-thermal part, visible in the form of striping, distorts compact sources and degrades the sensitivity. Since noise and signal spectral densities share the same frequency range, filtering techniques are inadequate except for point sources. The problem can be approached in two main ways: either by using a noise model and maximum-likelihood solver (Keihänen et al. 2004), or by devising an empirical tool to exploit the redundancy built in the scans.

The *Scanamorphos* public software (Roussel 2012) belongs to the second category and has been applied up to now to data from P-Artemis on APEX (André et al. 2008) and the PACS (Poglitsch et al. 2010) and SPIRE (Griffin et al. 2010) photometer arrays onboard Herschel (Pilbratt et al. 2010). The only assumption about the drifts consists in considering a minimum timescale below which they will not be corrected (ideally corresponding to their knee frequency), and the only requirement about the signal is its time invariance.

An advantage of the empirical approach is that results are immune to mismatches between noise models and realizations, and robust with respect to calibration and pointing errors. As no instrument model is relied on, an added benefit is to allow the calibration of some instrumental properties, based on science observations. In particular, *Scanamorphos* was used to calibrate the relative beam areas of the SPIRE photometer arrays (using bright extended emission from star formation regions), and provided an independent confirmation of the flat-field corrections derived by the PACS Instrument Control Center. The principles are intuitive and easy to understand, and the modularity allows subtle effects to be progressively incorporated.

The memory requirements of this class of tools induce a technical difficulty: the full history of all detectors is simultaneously needed, unless the field of view can be sliced into several blocks, then processed separately. However, the required level of redundancy is low for space observations, and several square degrees mapped with the blue array of PACS (2048 detectors) can be processed in one block with less than 48 Gb of memory.

For more details than is practical to give here, the reader is directed to the online documentation¹.

2 Principles

For Herschel, scan observations are performed as sketched in Figure 1a. In the most common case, there is an even number of scans, half in a given orientation and the other half in the perpendicular orientation, but neither the parity nor the orthogonality are mandatory. A typical weight map (number of samples weighted by the fractional area of each detector and its inverse square white noise) looks like Figure 1b. The level of redundancy per scan is of the same order for all Herschel arrays operated at the same scan speed, within a factor two.

¹ Institut d'Astrophysique de Paris, Université Pierre et Marie Curie (UPMC), CNRS (UMR 7095), 75014 Paris, France

ⁱavailable at: <http://www2.iap.fr/users/rousseau/herschel/>

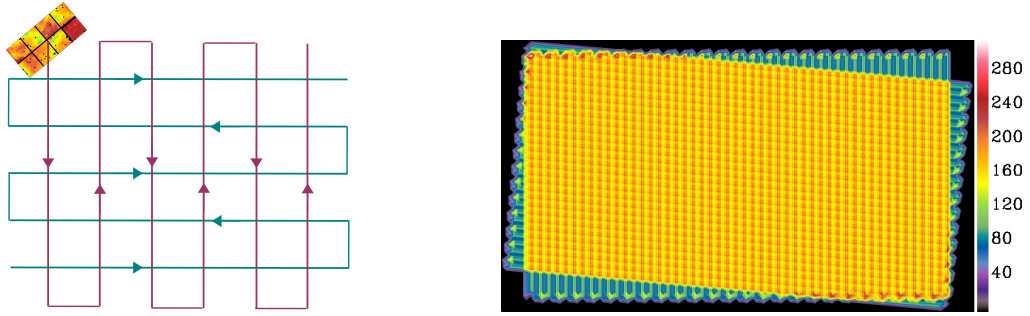


Fig. 1. Left: Schematic representation of a scan observation with the PACS blue array (made of eight 256-pixel subarrays). The colored lines show the trajectory of a detector in two orthogonal scans. There can be several repetitions of each orientation. **Right:** Weight map of a PACS observation combining 2 scans, projected on pixels of size FWHM (for the default final size of FWHM/4, the average coverage is of the order of 10 samples per pixel per scan pair).

The map size determines a boundary between long timescales (longer than the scan leg duration), that are not sampled properly by the observations, and short timescales, that do not require any assumption on the large-scale structure, contrary to the former. Drifts are first subtracted on the longest timescales (where their power spectral density is the largest), as linear baselines. The redundancy is used to determine time series that are coherent (producing the same map to first order) for all bolometers and all scans. The solution is not unique, but the aim is to preserve as well as possible genuine sky gradients. The algorithm is thus slightly different for fields containing bright extended emission, in which case the sky gradients can be comparable to the artificial gradients resulting from the thermal drift (Fig. 2). These two types of gradients can be separated owing to the strategy of scanning the sky at two very distinct scan angles. The process is iterative, building a new reference map after each step, applying an adaptive mask to the brightest sources and using robust linear fits. Once zero-order baselines have been subtracted, residual baselines are defined as the linear fit of the difference between the signal recorded by each bolometer and the signal simulated from the reference map. These residuals are subtracted from the data at each iteration, until the process converges.

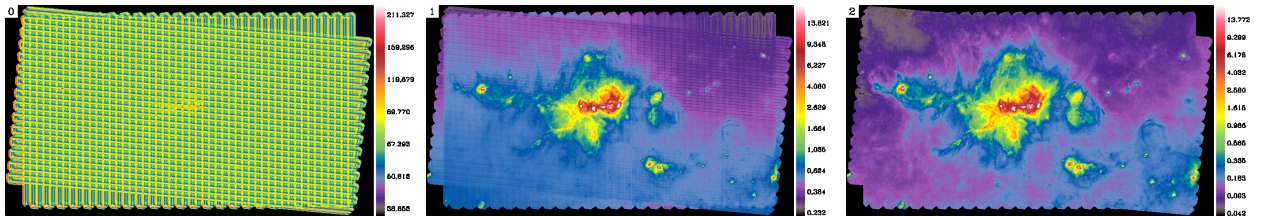


Fig. 2. Illustration of the drift subtraction on timescales above the scan leg crossing time, with the constraint of preserving genuine sky gradients. The target is the NGC 6334 star formation region (Russeau et al. 2012) from the HOBYS program (Motte et al. 2010). **Left:** Raw data. **Middle:** After subtraction of zero-order baselines (offsets). **Right:** After subtraction of linear baselines making use of the redundancy (destriping).

The correction for drifts on shorter spatial scales is based on the choice of a stability length l_s , within which the drifts are assumed constant and the signal uniform. An explicit mechanism is thus implemented to protect compact sources and sky gradients within l_s . This length is chosen equal to the average beam full width at half maximum (FWHM) by default, and increased if necessary, so that one can compute basic statistics from the samples of a bolometer crossing l_s . New spatial and temporal grids adapted to the problem are then set up, based on l_s and its crossing time T_c at the given scan speed.

Short-timescale drifts are decomposed into the drift averaged over all bolometers (abusively called thermal drift for convenience, since the latter is strongly correlated) and the individual drifts, that are uncorrelated (i.e. the flicker noise). The average drift is subtracted first, and the individual drifts subsequently. The signal recorded at time t by the bolometer b_i is described as:

$$R(t, b_i) = S(p) + \bar{D}(t) + D_{b_i}(t) + HF(t, b_i)$$

where $S(p)$ is the sky brightness in the pixel p sampled by b_i at time t , \bar{D} is the average drift, D_{b_i} is the individual drift of bolometer b_i , and HF is the high-frequency noise (white noise and glitches).

In each pixel of size l_s , the contributing samples are grouped in distinct bolometer crossings, and crossings that have too few samples are rejected. A test is then applied to determine whether the assumption of signal uniformity is valid or not, by comparing the dispersion of each crossing with a noise threshold, computed from the spectral density of the relevant bolometer. If more than a predefined small fraction of the dispersions are higher than the thresholds, the pixel is likely to contain non-uniform emission, and no drift correction is computed. In the opposite case, only crossings with elevated dispersions (possibly affected by glitches) are rejected. Pointing corrections are then applied to the valid crossings, using the map built at the previous iteration, to cancel brightness differences caused by the different trajectories of the detectors within the pixel.

For the average drift, differences between pairs of crossings $\delta(t_{c_1}, t_{c_2}) = R(t_{c_1}, b_i) - R(t_{c_2}, b_j)$ are computed, and for each time pair projected on the coarse time grid (t_{c_1}, t_{c_2}) , they are coadded regardless of the bolometers involved and the position on the sky:

$$\delta(t_{c_1}, t_{c_2}) = \bar{D}(t_{c_1}) - \bar{D}(t_{c_2}) + \text{WM}_{p,i,j} [D_{b_i}(t_{c_1}) - D_{b_j}(t_{c_2})]$$

where WM stands for the weighted mean running on all pixels p and bolometers crossing p at times t_{c_1} and t_{c_2} . The high-frequency noise vanishes in the coaddition and, since the individual drifts are uncorrelated, the WM term is also negligible provided the redundancy is sufficient. The coadded δ terms thus reduce to differences between the average drift at distinct times, $\bar{D}(t_{c_1}) - \bar{D}(t_{c_2})$. From the matrix of these differences, it is possible to reconstruct the absolute average drift as a function of time, using an iterative process. The solution is not unique: it is the superposition of the true average drift and an excess component, that has the same periodicity as the spatial coordinates (Fig. 3). To subtract the latter, we exploit the fact that it produces the same map for all successive scans (whereas the true drift never repeats itself), and has smoother variations.

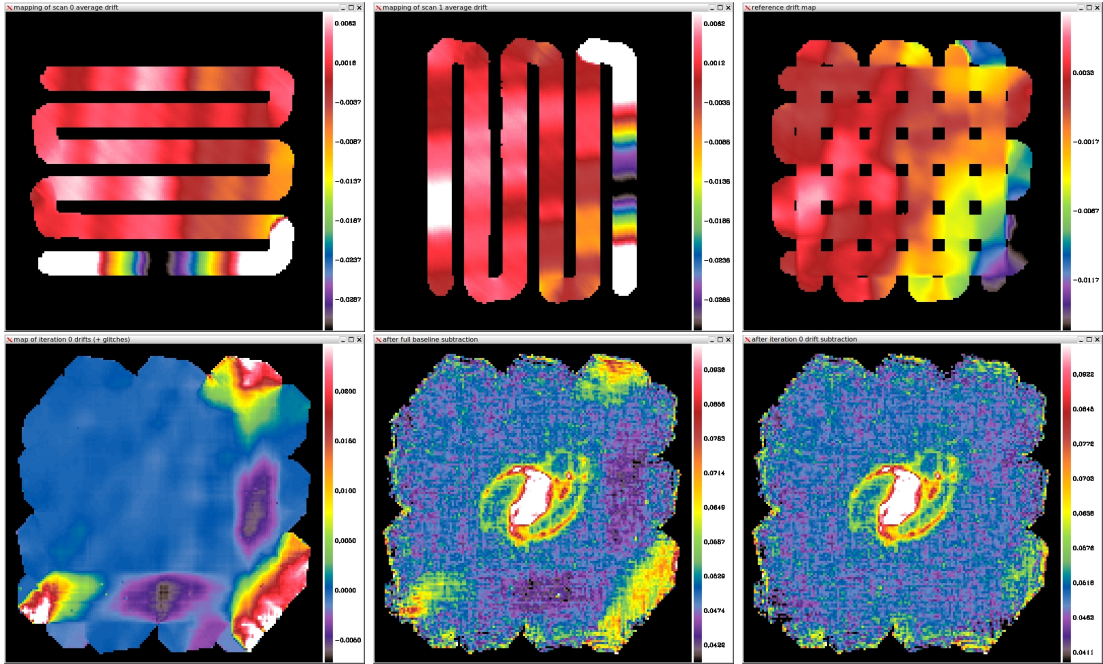


Fig. 3. Subtraction of the thermal drift, shown on an example where its effects are easy to see: a PACS observation of NGC 1097 from the KINGFISH survey (Kennicutt et al. 2011). The calibration frames taken before the scientific observations cause strong transients on two edges of the map. **Top left and middle:** Projections of the raw average drift computed from the $\bar{D}(t_{c_1}) - \bar{D}(t_{c_2})$ matrix, in the first scan (among 3) of each scanning direction. **Top right:** Projection of the excess drift. **Bottom left:** Projection of the true (raw - excess) average drift. **Bottom middle and right:** Maps of NGC 1097 before and after the average drift subtraction (on a coarse pixel grid).

For individual drifts, the difference between each crossing and the average of all valid crossings is computed:

$$\Delta(t_c, b_i) = R(t_c, b_i) - \text{WM}_j [R(t_c, b_j)] = \bar{D}(t_c) + D_{b_i}(t_c) + HF(t_c, b_i) - \text{WM}_j [\bar{D}(t_c) + D_{b_j}(t_c)].$$

Since the average drift has been previously subtracted at all times, and given that the individual drifts are uncorrelated, $\Delta(t_c, b_i)$ reduces to the sum of the individual drift of bolometer b_i and its white noise binned on the coarse time grid. In practice, the redundancy is increased and the errors decreased when the corrections are first binned into much larger time intervals than T_c ; the results are significantly improved in this case, as shown by Figure 4. For both the average drift and the individual drifts, the convergence is reached when the amplitude of the subtracted drifts has become smaller than the white noise for most bolometers.

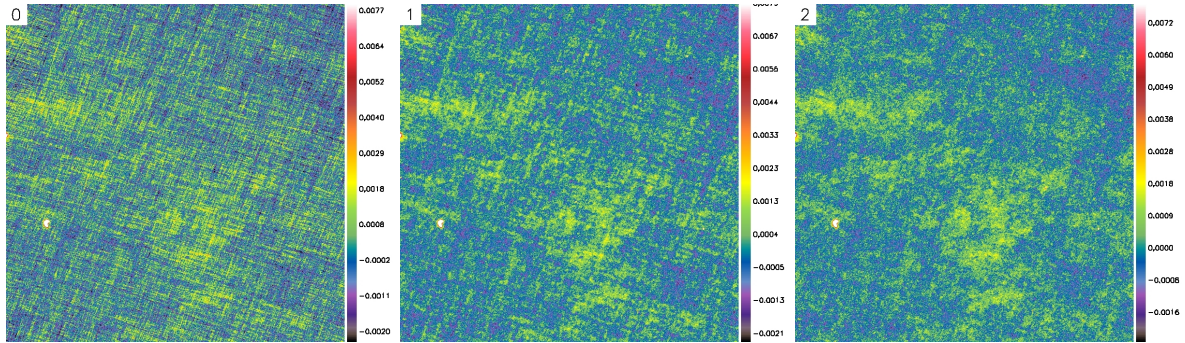


Fig. 4. Effect of performing the individual drift subtraction on various timescales, illustrated on a PACS observation from the HEVICS survey (Davies et al. 2010). The extracted image is about 2.2 degrees on a side and the displayed brightness range emphasizes very diffuse structures. **Left:** The drifts have been subtracted only on the longest timescales (above the scan leg crossing time). **Middle:** The subsequent iterations to subtract the drifts all have the minimum time step T_c . **Right:** They have successive time steps of $3^n \times T_c$, with integer $n = 3$ to 0.

3 Example

Abundant visualizations of the different processing steps and simulation results are given in the companion paper (Roussel 2012). Let us remark that the amplitude of the individual drifts is low in SPIRE data, but of much higher amplitude with respect to the signal and white noise in PACS data. The PACS instrument is also affected by additional artefacts. The efficiency of the algorithm is thus best demonstrated on PACS data (but SPIRE data also make interesting test cases when they are affected by a so-called “cooler burp”, i.e. an abrupt variation of the thermal drift slope as a function of time).

Here, we very briefly compare **Scanamorphos** with the two softwares that are fully implemented in the PACS pipeline, i.e. **PhotProject**, subtracting the low-frequency noise by means of a highpass filter applied after masking the source, and **MADmap**, a maximum-likelihood solver initially developed for CMB experiments (Cantalupo 2010), and adapted to the Herschel pipelines. We take as an example the galaxy M 82, observed as part of the Very Nearby Galaxies Survey (guaranteed time; P.I. C. Wilson). This target is chosen because its starbursting nuclear regions and dusty halo offer wide ranges of characteristic lengths and brightnesses, that are challenging for some classes of processing tools. Figure 5 shows the results and illustrates the advantages of using **Scanamorphos**. They can be succinctly summarized as follows: diffuse structures are not filtered, low-frequency noise is adequately subtracted even when superposed to an extended signal, and bright compact sources do not generate any distortions.

4 Concluding remarks

The main task of **Scanamorphos** is to correct for the brightness drifts caused by any type of additive low-frequency noise, using the redundancy built in scan observations. Other natural tasks of the same software are the masking of detector instabilities and glitches, since redundancy is necessary to distinguish these artefacts from real signal. The method outlined here is always applicable provided scans can be sliced into distinct scan legs (specifically for the destriping on the largest timescales, not for the drift subtraction on shorter timescales), and as long as there is as much redundancy as in Herschel observations (Fig. 1), even though an insignificant fraction of the field of view is covered by any single bolometer.

On the ground, the thermal drift is dominated by atmospheric fluctuations, occurring on smaller timescales than the drift originating in small temperature variations of the telescope and cryogenic bath. Consequently, the

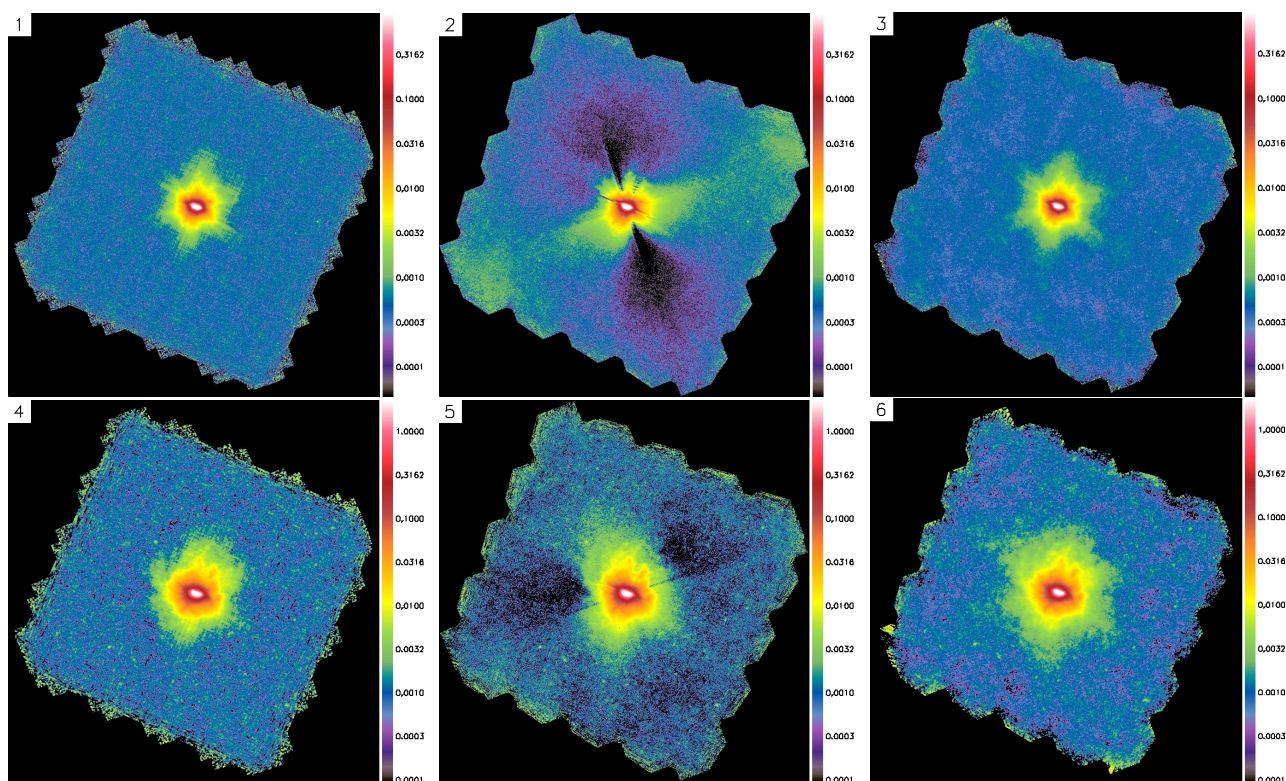


Fig. 5. Results of processing the PACS data of M 82 at $70 \mu\text{m}$ (top row) and $160 \mu\text{m}$ (bottom row) with three different tools. **Left:** PhotProject (1 and 4). **Middle:** MADmap (2 and 5). **Right:** Scanamorphos (3 and 6). The brightness scale (in Jy/pixel) is logarithmic and emphasizes faint structures.

method exposed above to subtract the average drift can be employed only if the sampling rate is high enough to allow a workable stability time T_c . For Herschel observations, it can take the values 5, 10 and 18.6 Hz, depending on the array and observing mode. In practice, it should be higher than a few times the knee frequency of the drift. Otherwise, either the data will remain heavily contaminated by the high-frequency component of the thermal noise, or it will be possible to restore only compact sources (i.e. much smaller than the array) by filtering the data. There is no such limitation for the uncorrelated drifts, because they are determined by detector and readout physics, and usually have smaller knee frequencies.

I am grateful to all the colleagues, too many to cite, who indirectly contributed to the continuous development of the software, by offering pieces of code to format the input data, expertise on the PACS and SPIRE instruments, test data pre-processed up to level 1, useful suggestions of new functionalities, and/or (last but not least) bug reports that were key in improving the code.

References

- André, P., Minier, V., Gallais, P., et al. 2008, *A&A*, 490, L27
 Cantalupo, C.M., Borrill, J.D., Jaffe, A.H., Kisner, T.S., & Stompor, R. 2010, *ApJS*, 187, 212
 Davies, J.I., Baes, M., Bendo, G.J., et al. 2010, *A&A*, 518, L48
 Griffin, M., et al. 2010, *A&A*, 518, L3
 Keihänen, E., Kurki-Suonio, H., Poutanen, T., et al. 2004, *A&A*, 428, 287
 Kennicutt, R.C., et al. 2011, *PASP*, 123, 1347
 Motte, F., Zavagno, A., Bontemps, S., et al. 2010, *A&A*, 518, L77
 Pilbratt, G.L., Riedinger, J.R., Passvogel, T., et al. 2010, *A&A*, 518, L1
 Poglitsch, A., Waelkens, C., Geis, N., et al. 2010, *A&A*, 518, L2
 Roussel, H. 2012, <http://arxiv.org/abs/1205.2576>
 Russeil, D., Schneider, N., Anderson, L. D. et al. 2012, submitted to *A&A*